Bi-functional Interfaces by Poly-Ionic Liquid Treatment in Efficient *pin* and *nip* Perovskite Solar Cells

Pietro Caprioglio[a,b], Daniel Saul Cruz[c], Sebastián Caicedo-Dávila[d], Fengshuo Zu[e], Albertus Adrian Sutanto[f], Lukas Kegelmann[b], Christian M. Wolff[a], Lorena Perdigón-Toro[a], Norbert Koch[e], Bernd Rech[g], Giulia Grancini[f,i], Daniel Abou-Ras[d], Mohammad Khaja Nazeeruddin[f], Martin Stolterfoht[a], Steve Albrecht[b,h], Markus Antonietti[c] and Dieter Neher[a]

[a] Institute of Physics and Astronomy, University of Potsdam, 14476 Potsdam, Germany
[b] Young Investigator Group Perovskite Tandem Solar Cells, Helmholtz-Zentrum Berlin für Materialien und Energie GmbH, 12489 Berlin, Germany
[c] Max Planck Institute of Colloids and Interfaces, Am Mühlenberg 1, 14476 Potsdam, Germany
[d] Helmholtz Zentrum Berlin für Materialien und Energie GmbH, 12489 Berlin, Germany
e Humboldt University, Institut f¨ur Physik, Newtonstraße 15, 12489 Berlin, Germany
f Group for Molecular Engineering of Functional Materials, Institute of Chemical Sciences and Engineering, École Polytechnique Fédérale de Lausanne, CH-1951 Sion, Switzerland
[g] Institute for Silicon Photovoltaics, Helmholtz-Zentrum Berlin für Materialien und Energie GmbH, 12489 Berlin, Germany
[h] Faculty IV – Electrical Engineering and Computer Science Technical, University Berlin, 10587 Berlin, Germany
[i] Department of Chemistry, University of Pavia, Via Torquato Taramelli 14, 27100 Pavia, Italy

Abstract

A large number of methodologies have been explored in perovskite solar cells to boost efficiency and stability. However, most of the approaches address particularly one singular problematic in a specific device configuration. In the present work, we utilize a poly(ionic-liquid) (PIL) to modify the surface of the perovskite material and to create a bi-functional interlayer in devices. These solar cells exhibit outstanding V_{OC} and FF values of 1.17 V and 83% respectively, resulting in conversion efficiencies up to 21.4%. The presence of the PIL at the perovskite surface reduces the non-radiative losses down to 60 meV already in the neat material, suggesting surface trap passivation, thereby pushing the external photoluminescence quantum yield up to 7%. In devices, the PIL treatment induces a bi-functionality of the surface where insulating areas act as a blocking layer reducing interfacial charge recombination and increasing the V_{OC}, whereas, at the same time, the neighbouring regions provide more efficient charge extraction, increasing the FF. The PIL-treated devices additionally show enhanced stability under maximum power point, allowing to retain unchanged efficiencies after 10 months of shelf storage. With this novel approach, exclusively addressing the perovskite surface, we manage to efficiently suppress the non-radiative recombination of charges, promote the charge extraction and improve the stability at once. Finally, we expanded this methodology to nip cells, confirming the generality of this treatment and opening the possibility for the potential usage of this material in various cell architectures, perovskite compositions, as well as in tandem devices.

Introduction

In recent years, the research field of photovoltaics (PV) has been preponderantly overturned by the advent of hybrid organic-inorganic halide perovskites. This class of materials attracted the attention of the academic and industrial fields due to their sky-rocketing power conversion efficiencies (PCE) (>25%), intriguing material properties[1–3] and promising low-cost production.[4,5] Halide perovskites benefit from a high absorption coefficient, panchromatic absorption of light[6], long carrier diffusion length[7,8] and shallow trap energy levels.[1] The combination of these properties allows for a high photocurrent and low non-radiative recombination with high (external) photoluminescence yields (>20%).[9] Despite the tremendous improvements that this technology witnessed during the last decade[10], perovskite solar cells (PSCs) have not yet reached their theoretically predicted efficiencies[11] and still suffer from long-term stability issues.[12] In particular, *pin* devices, which currently dominates the tandem research, lack behind their *nip* counterparts in terms of efficiency and stability. Currently, researchers around the world are addressing these problematics in order to exploit the full potential of this class of materials and to achieve stable devices, suitable for a desirable industrial production. Through the years, diverse approaches have been introduced with the purpose of increasing the PCEs of perovskite PV. For instance, several works focused on reducing the energy losses in the devices and consequently increasing the open-circuit voltages (V_{OC}) by using passivating agents[9,13,14], introducing interlayers[15,16] or by surface modifications.[17] Other approaches, instead, focused directly on improving the material quality through compositional engineering[18–20] or by the usage of additives.[21,22] Finally, work has been devoted to the optimization of the charge transport layers (CTLs) by minimizing transport losses or reducing the energetic offset between the layers.[23,24] On the other hand, various methodologies have been implemented aiming to improve the intrinsic stability of the material, as well as devices. For example, low-dimensional (2D) perovskites,[25–27] or a combination of high and low dimensional structures,[28,29] have been successfully implemented improving the water and humidity resilience, while also hindering the out-diffusion of volatile organic cations, and finally leading to significantly improved long-term stability.[30] Other successful approaches allowed for better device stability by implementing self-assembled amphiphilic monolayers (SAMs)[31–33] or by sandwiching the perovskite between diffusion and water resistant layers[34–36], blocking the penetration of water and oxygen and the diffusion of the organic cation at the same time.

In this work, we introduce a novel approach to concomitantly increase the efficiency and the stability of different PSCs by treating the perovskite surface with a poly(ionic-liquid) (PIL). In the past, a large number of studies dealt with the implementation of ionic liquids in perovskite solar cells, either as additives in the perovskite precursor solution to improve the material quality and stability[37–40] or as contact work-function modifier[23,41–43] to enhance charge collection. On the other hand, the usage of the polymeric version of this class of material as post treatment of halide perovskites has not been explored yet. Polymer ionic liquids are "liquid", i.e. their glass transition temperature is below room temperature, and as that, they are ion conductors which form a conformal coating on surfaces by spreading down even to nanometer dimensions. Conceptually, this coating not only protects the surface, but also provides charge stabilization (by other charges) and lowering of interface resistance and impedance. PILs are also known to be extremely versatile due to the interchangeability of the

counterion, allowing them to achieve high ionic conductivity, hydrophobicity, thermodynamic and thermal stability, as well as chemical durability.[44,45] Here, we employ an imidazolium-based PIL with a bis(trifluoromethane)sulfonimide (TFSI) counterion, abbreviated as [PeIm][TFSI], to modify the interface between a triple cation perovskite and a C_{60}-based electron transport layer (ETL). We show that the PIL assembles primarily on the perovskite surface, where it reduces non-radiative losses in the neat material as well as in the complete cell. Detailed microscopic studies reveal the presents of extended areas where the PIL acts as blocking layer between perovskite and C_{60}, preventing interfacial non-radiative recombination and thus, increasing the V_{OC} of the device. On the neighbouring areas, the modified interface promotes the extraction of charges and provides a more ideal energy alignment between the layers, resulting in extraordinary high *FF* values. Additionally, the hydrophobic nature of the PIL counterions and the passivating behaviour of the PIL improves the stability of the device under maximum power point tracking and long-term shelf storage. Finally, we demonstrate the beneficial effect of the PIL in *nip* cells where the treatment modifies the interface between the perovskite and a Spiro-OMeTAD-based hole transport layer (HTL), increasing the *FF* and enhancing the reproducibility.

Results and Discussion

Our work focuses primarily on optimized *pin*-type devices,[46] in which the semiconducting polymer poly[bis(4-phenyl)(2,4,6- trimethylphenyl)amine] (PTAA) serves as the hole-transporting material in the device architecture: indium tin oxide, ITO (150 nm)/PTAA (8 nm)/ poly[(9,9-bis(30- ((N,N-dimethyl)-N-ethylammonium)-propyl)-2,7-fluorene)- alt-2,7-(9,9-dioctylfluorene)] dibromide (PFN-P2)/ perovskite (400–500 nm)/C_{60} (30 nm)/bathocuproine, BCP (8 nm)/Cu (100 nm).The perovskite absorber has the composition $(Cs_{0.05}(MA_{0.17}FA_{0.83})_{0.95})Pb(I_{0.83}Br_{0.17})_3$, with an optical bandgap of 1.62 eV. [47] The PIL is introduced between the perovskite and the C_{60} layer, as depicted in Fig. 1a) by spin coating a highly diluted solution (0.5 mg/ml in acetonitrile:isopropanol (1:4)) on top of the perovskite. After that, the device is completed by depositing C_{60}, BCP and Cu by thermal evaporation, see Fig.1 a). The positive effect of the PIL treatment on power conversion efficiency is exemplified in the current-voltage (*J-V*) characteristics in **Fig. 1b**, where a parallel improvement of the V_{OC} and the *FF* is observed. Notably, the treated cells do not present any significant hysteresis behaviour, **Fig. S1A (SI)**. The increase of the V_{OC}, reaching values up to 1.17 V, suggests that the presence of the PIL reduces the non-radiative recombination of charges at the interface between the perovskite and the C_{60}.[48] Moreover, the *FF* increases to outstanding values of nearly 83%, indicating that the PIL improves the charge extraction and reduces the transport resistance.[49] The average *FF* values averaged over a large number of devices plotted in **Fig. 1c** increases from below 77% for the reference cells to nearly 81% for the PIL containing ones. **Fig. 1c** also denotes a large improvement of the reproducibility of the device performance of the PIL-containing devices, which results also in a smaller spread of the J_{SC} values. The combination of the improved V_{OC} and *FF* results in an efficiency enhancement from an averaged PCE of 19% for the reference cells to an average PCE of nearly 21%, again with a more narrow distribution. The best device, **Fig. S1B (SI)** reaches a PCE of 21.4%, which is among the best ever reported for *pin*-type PSCs.[50,51] We note that the introduction of the PIL

treatment does not affect the EQE_{PV} nor the absorption, **Fig. 2A-2B (SI)**, thus not influencing the bandgap of the perovskite absorber. To disproof that the improvement comes from just one of the two species of the PIL, in **Fig. S1C (SI),** we compare cells with imidazolium-based PILs using different counterions, namely [PeIm][Br] and [PeIm][PF_6]. Interestingly, [PeIm][Br] limits the performance of the device, whereas [PeIm][PF_6] gives identical results to the [PeIm][TFSI]. This finding suggests superior effects of fluoride containing hydrophobic anions over (hydrophilic) halides as counterions, consistent with earlier results[40], but may also imply that the improvement of the [PeIm][TFSI] does not come from only one of the two constituents.

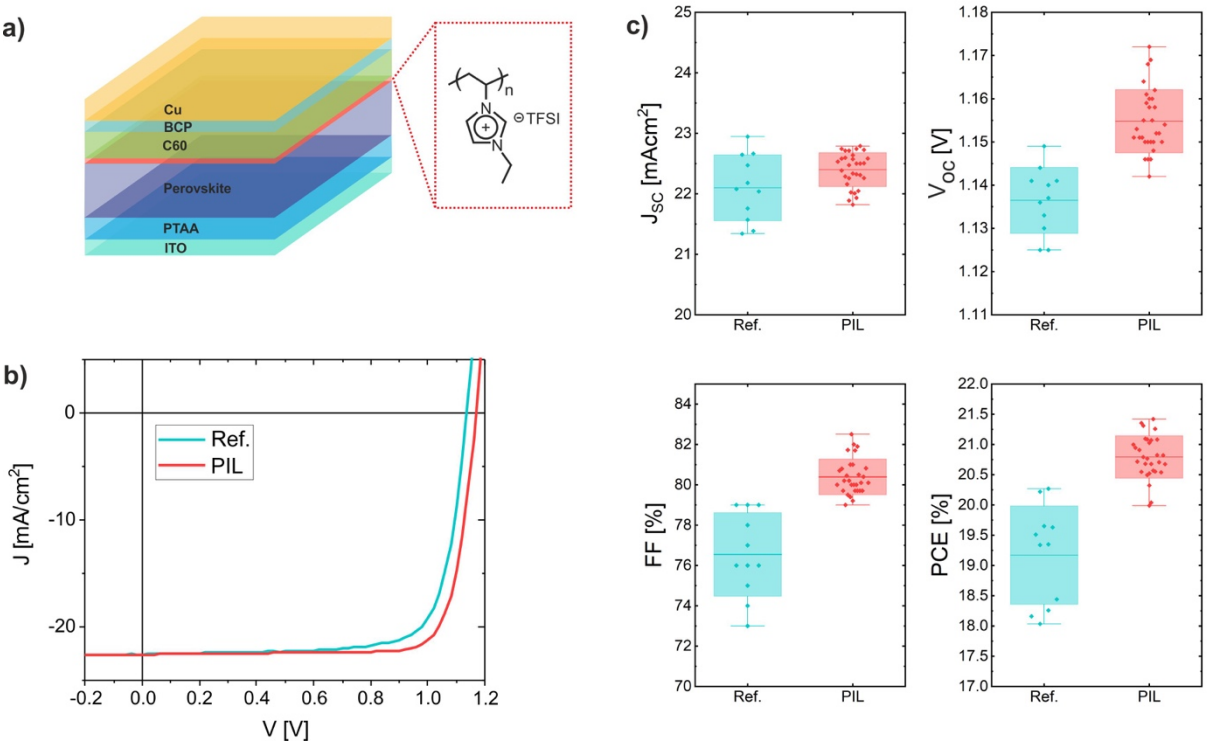

Figure 1: *a) Pin-type device layer structure with highlighted chemical structure of the poly(ionic-liquid) (PIL) layer inserted between the perovskite and the C_{60}. b) Typical current-voltage characteristic for a reference untreated cell and for a PIL-modified cell in reverse scan at 0.025 V/s (hysteresis shown in Fig. S1A SI). c) Device parameter statistics for the reference cells and the PIL containing cells; the boxes indicate the standard deviation.*

In **Fig. S3A (SI)**, top surface scanning electron microscopy (SEM) images show that after spin coating the PIL, the typical cobblestone perovskite surface exhibits island-like features, which we assign to polymer aggregates. In **Fig. S4 (SI)**, X-ray diffraction (XRD) measurements indicate that the PIL surface treatment does not influence the crystal structure of the perovskite, nor additional phases were detected. However, contact angle measurements revealed that the PIL treatment induces an enhanced robustness of the perovskite surface in contact with water, as expected from the hydrophobic character of [PeIm][TFSI],[52] **Fig. S5 (SI)**. Energy-dispersive X-ray (EDX) elemental-distribution maps acquired on the surface of the PIL treated sample **(Fig. 2b-c**) confirm that these islands are composed of a carbon-rich material, presumably mostly the polymer [PeIm]. On the other hand, the O signal, not detectable in the reference sample, is attributed to the TFSI counter-ion (a more detailed discussion can be found in **Section 6**, **SI**) and its spatial distribution indicates that the mobile TFSI diffuses over the perovskite

surface. Additionally, EDX maps and line-scans of the cross-section of the PIL-treated sample in **Fig. 2g** exhibit higher concentrations of C and O on the surface of the film, indicating that both, the polymer and the counter-ion, do not diffuse into the perovskite layer. Notably, the reference sample does not present any O at the perovskite surface. As detailed in **Fig. S6A (SI)**, the O and C on the top surface appear to be anticorrelated, meaning that the PIL-modified surface features areas rich in the positively-charged polymer, surrounded by regions covered predominately by the TFSI anion. In **Fig. 2d-f**, comparative imaging of the surface with cathodoluminescence (CL) reveals a homogeneous increase in radiative efficiency upon surface treatment. The enhanced luminescence is visible both in the areas enriched by the TFSI counterion (**Fig. 2e**) and in the areas where the polyimidazole aggregates are detected (**Fig. 2f**). Here, small spots of enhanced luminescence originated by the perovskite underneath are visible through the pores of the covering non-emitting polymer islands (**Fig. S6B, SI**). Interestingly, in **Fig. 2e** the surface features small spots of increased luminescence, which are not present in CL maps of the neat perovskite. This suggests that trap passivation is more efficient at specific locations, which are uncorrelated with the morphology, as visible when the SEM and CL images are superimposed, **Fig. S6C (SI)**. Generally, this scenario indicates that both species contained in the [PeIm][TFSI] can effectively passivate surface defects preventing the non-radiative recombination of charges. Specifically, uncoordinated I, antisite PbI_3 as well as MA^+ or FA^+ vacancies can be passivated by the imidazolium groups.[40,53,54] Simultaneously, N and S can act as Lewis base and passivate I vacancies, uncoordinated Pb^{2+}, or metallic Pb clusters.[54–57]

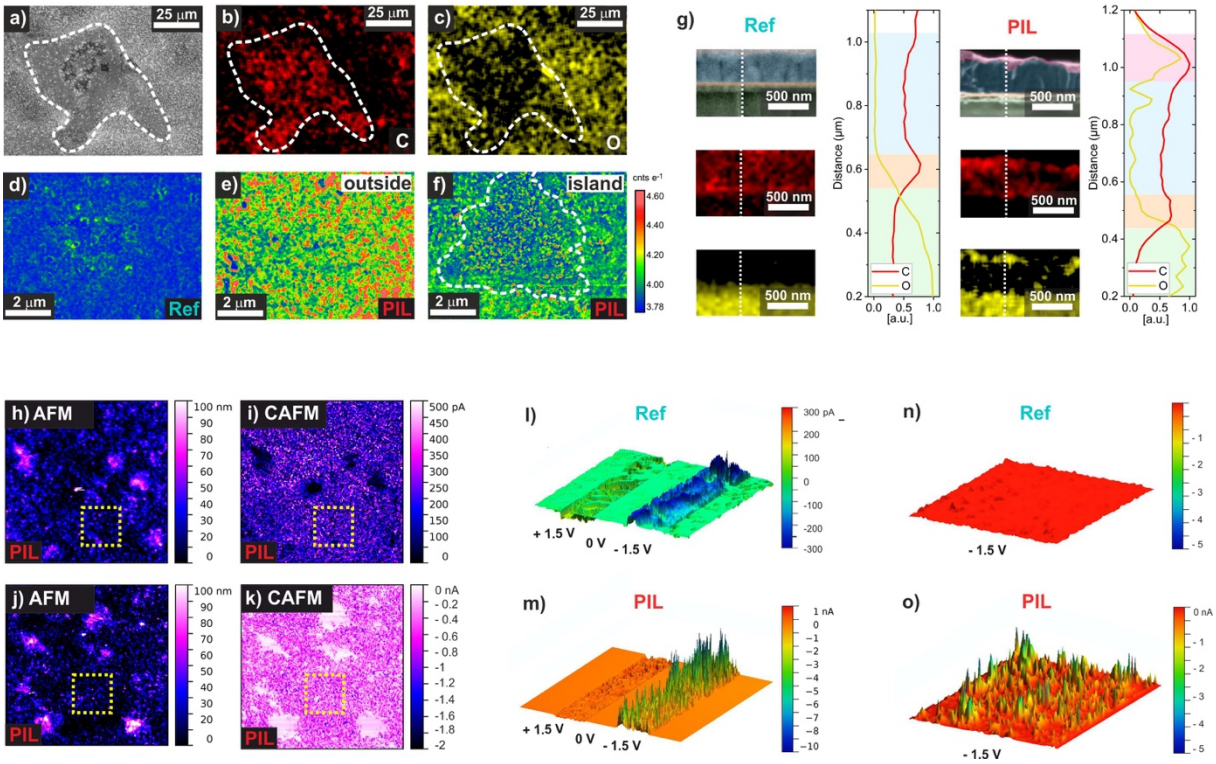

Figure 2: *a) SEM image showing a typical polymer-rich island on the surface of the perovskite (dashed contours). Corresponding EDX elemental-distribution maps for b) carbon and c) oxygen showing the enhancement and depletion of the signal on the island region, respectively. CL map of d) untreated perovskite film, e) PIL-treated film outside the polymer island and f) PIL-treated film on top of a polymer*

island. Notably, in f), luminescent spots are visible from the emitting perovskite beneath the non-emitting polymer island. g) SEM and EDX cross-section images for reference and PIL treated perovskite films with corresponding EDX line scans. For both samples, the C signal appears to be enhanced on the ITO/PTAA/perovskite interface, due to the PTAA. The O signal is concentrated on the glass region in both samples while the PIL-treated sample shows in addition the O signal at the surface indicating the presence of the TFSI molecules in that region. AFM topography images (40x40 μm^2) of reference and PIL-treated perovskite h) and j) show the presence of the polymer island, with heights between 50-100 nm. The corresponding CAFM images i) and k) reveal that the polymeric island presents a strong insulating character, reducing drastically the current signal when both a positive i) and a negative k) bias is applied. The dotted yellow lines indicate exemplary areas scanned in l)-o). l) 3D CAFM images (3x3 μm^2) of the untreated perovskite layer. The image represents a scan while applying different voltages from -1.5 V to 1.5 V in step-like fashion. m) 3D CAFM images (9x9 μm^2) of a perovskite layer treated with PIL. The image represents a scan with the same conditions of l). n) and o) shows 3D representations of two areas of 3x3 μm^2 with the same current scale to directly compare the reference perovskite and the PIL treated film upon applying a bias of -1.5V.

Atomic force microscopy (AFM) and conductive AFM (CAFM) analyses provide microscopic information on the correlation between surface topography and conductive properties (instrument configuration depicted in **Fig. S7A SI**). From large area surface scans, we observe that the reference sample exhibits a rather smooth topography and low uniform conductivity (**Fig. S7B, SI**). In contrast, the thick polymeric islands in the PIL treated surface, with a height of roughly 100 nm (**Fig. S7C, SI**), are highly insulting, as presented in **Fig. 2h-k**. Interestingly, the areas outside the islands show enhanced conductivity compared to the reference perovskite. To investigate this finding further, in **Fig. 2l-o** we performed CAFM measurements on these areas with higher spatial resolution, as indicated by the yellow lines in **Fig. 2h-k**. Here, the voltage (applied to the tip) is swept from positive to negative bias during the vertical scan in a step-like fashion. Surprisingly, while the reference samples exhibit low current signal (pA range), which is symmetric for positive and negative bias, the PIL treated surface demonstrates a tremendously increased current, approaching values of ~10 nA. Notably, the current enhancement is larger when the tip is biased negatively, namely electron injection at the top surface is more efficient compared to hole injection from the tip. Thereby, the improved electron transfer is in line with the higher *FF* of the PIL-treated device as the collection at the transport layer is facilitated. Interestingly, when CAFM images of the two samples are directly compared on an area of *3x3 μm^2* in the same current range, **Fig. 2c-d**, it is evident that the PIL treated surface features inhomogeneously distributed highly conductive points, which create isolated spikes in the current signal, reminiscent of the CL luminescence pattern. Also in this case, these spikes do not correlate with the surface topography, suggesting that a certain degree of surface modification is present on an atomic level and is not detectable by AFM or SEM. As proposed for other types of ionic liquids, the conductivity can be enhanced due to defect passivation of the surface.[58] In agreement with this, conductivity measurements, presented in **Fig. S8 (SI)** show that the PIL treated perovskite shows a 3 fold improvement in lateral conductivity and lower contact resistance compared to the reference perovskite. We will show that this property is not related to a higher net doping density in the perovskite layer. Consistently with this picture, the dark *J-V* characteristic of a series of actual devices, **Fig. S9 (SI)**, shows that the PIL treated samples present lower leakage current in the low voltage region,

indicating the presence of higher shunt resistance and a more ideal contact, also potentially increasing the *FF*.

The X-ray photoemission spectroscopy (XPS) survey spectrum of the PIL treated perovskite presents all the expected core level peaks of the characteristic elements present in both the neat perovskite and the neat PIL (**Fig. S10A, SI**). Moreover, high-resolution XPS measurements, presented in **Fig. 3a**, show that the deposition of the PIL on top of the perovskite surface induces a shift in all core levels of the perovskite elements towards lower binding energies by about 0.2 eV compared to the reference sample. Notably, in **Fig. 3b** the valence band spectra confirm the shift of the valence band maximum (VBM) closer to the Fermi level for the PIL treated perovskite. This result suggests that the PIL reduces the *n*-type character of the surface compared to the reference perovskite. It is reasonable to assume that the passivating behaviour can eliminate defects or impurities at the very surface, potentially responsible for the *n*-type character.[59] Surprisingly, the upwards shift in the VBM towards the Fermi level does not translate into a corresponding increase of the work function (WF). Such a scenario is only possible if the PIL, additionally to the reduction of the n-doping at the surface, creates a surface dipole pointing towards the vacuum. This phenomenon is associated to the nature of the polyionic liquids, where the arrangement of the two ions induces a Maxwell-Wagner-Sillars type interfacial polarization.[60,61] Next, to understand the impact of the PIL on the energetic alignment with respect to the C_{60} ETL, UPS measurements were performed on samples with 20 nm of C_{60} deposited on top, **Fig. 3d**. The resulting interfacial energy diagram is depicted in **Fig. 3c**. It is evident that the PIL-treated perovskite film exhibits a better alignment of the perovskite conduction band edge with the lowest unoccupied molecular orbital (LUMO) of the C_{60} layer, promoting charge extraction by eliminating the small extraction barrier found for the reference sample. Additionally, the surface dipole introduces a downwards shift of the highest occupied molecular orbital (HOMO) of the C_{60} with respect to the VBM of the PIL-treated perovskite, improving the contact selectivity. Overall, we observe that the application of the PIL besides passivating the surface traps also provides a better energy allignment, beneficial in terms of increased *FF* due to better charge extraction.

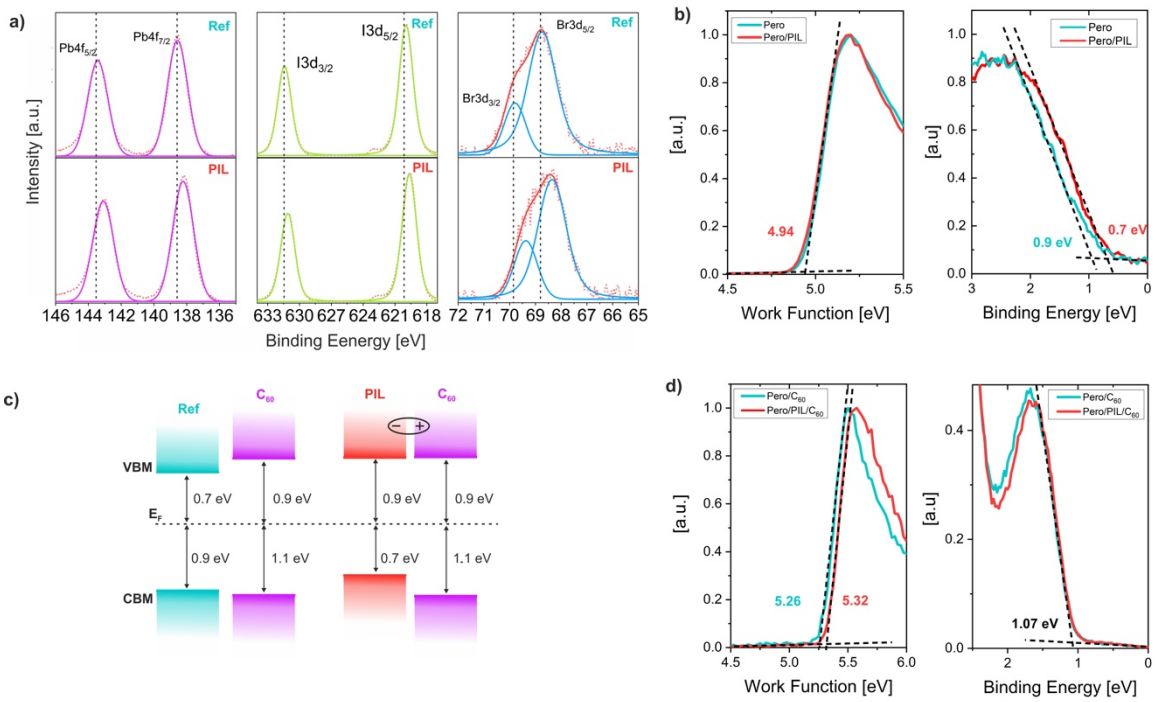

Figure 3: *a) High resolution XPS spectra of perovskite films with and without PIL treatment for characteristic perovskite elements to highlight the core level shifts. b) Ultraviolet photoelectron spectroscopy (UPS) results for work function and valence bands (probed by X-ray) of the reference and PIL treated neat perovskite and c) with C_{60} films on top of the perovskite layer with and w/ PIL treatment. c) Interfacial energy levels of the perovskites/C_{60} interfaces as obtained from the photoemission spectroscopy data shown in panel (b) and (d). Note, all perovskite films were deposited on top of ITO/PTAA substrates and UPS as employed here probes only the surface energetics of the studied sample*

The experimental results collected so far reveal that the PIL treatment enhances the transfer of charges across the neat perovskite surface while also improving the energy alignment at the perovskite/C_{60} junction, both being beneficial for a high *FF* of the PIL-containing devices. Next, we address the increased V_{OC} of PIL treated samples. As shown in **Fig. 4a-b,** the analysis of the photoluminescence of the neat films and the complete cells reveals a significant reduction of non-radiative recombination in the PIL-treated samples. We find that the photoluminescence quantum yield (*PLQY*) of the bare material increases from 1.2% for the reference sample to 7.2% for the PIL treated one. Following the approach presented in **Section S11 (SI)** and in previous works,[62,63] by combining the information from *PLQY* measurements and the *EQE* spectra allows to calculate the quasi-Fermi level splitting (*QFLS*) in the absorber, and relate this to the thermodynamic radiative limit for these cells. The latter is found to be ~1.32 eV for both samples. The *QFLS* in the neat material essentially corresponds to the maximum achievable V_{OC} for a given perovskite and illumination condition. We find that the *QFLS* increases from ~1.20 eV to ~1.26 eV for the PIL-treated perovskite, indicating that the non-radiative losses in the neat material are reduced from 120 meV to 60 meV. This substantial reduction in non-radiative recombination is qualitatively consistent with the increase in CL emission, where the passivation of the PIL is visualized on the surface. Moreover, in full devices, the *PLQY* of the treated sample increases from 0.1% to nearly 0.5%, increasing the

QFLS from 1.14 eV to 1.18 eV, in good agreement with the measured V_{OC} of the cells (1.14 V and 1.17 V, respectively). Consequently, the total non-radiative losses in the complete device are reduced from 180 meV to 140 meV. Consistently, the electroluminescence efficiency (EQE_{EL}) presented in **Fig. S12 (SI)** exhibits a more than a two-fold increase for the PIL treated device. These results highlight the beneficial effects of the newly-formed perovskite/PIL/C_{60} junction, where interfacial non-radiative recombination is reduced, allowing for higher *QFLS* and V_{OC}. In particular, the insulating polymer islands act as a blocking layer, spatially separating the holes in the perovskite from the electrons on C_{60} and decreasing the possibility for non-radiative recombination of charges across this interface. In agreement with this picture, the photoluminescence decays (TRPL) in **Fig. 4c** show that the neat perovskite and the perovskite covered with C_{60} exhibit longer decays when they are treated with PIL. By fitting the decay with a double exponential model and extracting the lifetime from the slower component characteristic for SRH recombination,[48] upon PIL treatment the lifetimes increase from 400 ns to 900 ns for the neat material and from 60 ns to 110 ns for perovskite/C_{60} junction. Interestingly, this reduction in interfacial non-radiative recombination does not translate in a change in ideality factor, which is found to be 1.35 for both samples (**Fig. S13, SI**).

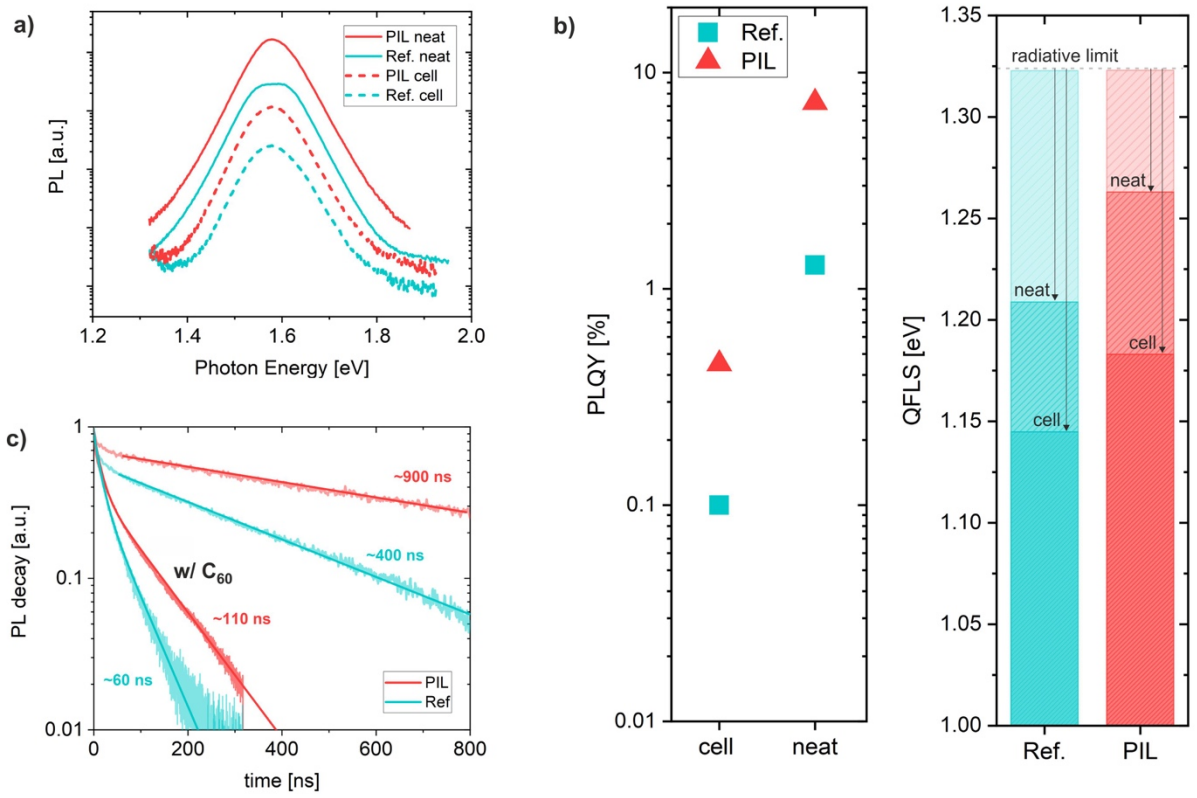

Figure 4: *a) Photoluminescence spectra of the neat perovskite and complete cells for the reference and the PIL-treated samples. b) Photoluminescence quantum yield measured on the neat material and the complete device stack with the respective calculated quasi-Fermi level splitting. The calculated radiative limit is shown to highlight the energy losses with respect to the theoretical thermodynamic limit. c) Normalized TRPL decays of the reference and the PIL-treated perovskite, with and without C_{60} deposited on top. In both cases the PIL-treated samples show longer lifetimes denoting an effective reduction of non-radiative recombination.*

Remarkably, introducing the PIL in the device stack does not only improve of the material quality and the device performance, but also the stability of the devices. We find that non-encapsulated device comprising the PIL exhibit significantly increased stability under maximum power point (MPP) tracking in inert atmosphere as compared with the reference cell. Notably, the PIL treated cell retains 90% of its initial efficiency after more than 90 h at 50° C, as presented in **Fig. 5 c)**. Moreover, PIL treated non-encapsulated devices stored under inert atmosphere and exposed to indoor light can fully retain their PCE of ~21% during 10 months of shelf storage, as exemplarily shown in **Fig. 5 a)** and **b)**. A larger set of devices aged for up to 15 months is presented in **Fig. 5 d),** demonstrating that the PIL-treated devices exhibit a longer shelf life compared to the reference devices, which degrade significantly over time. The improved stability may originate from two main factors. On one hand, the new hydrophobic surface induced by the PIL treatment helps to prevent the penetration of water and moisture, which leads to degradation of the perovskite material. On the other hand, the PIL layer improves the stability of the perovskite from a structural point of view. As proposed in previous studies, the presence of surface defects and trapped charges can accelerate moisture, oxygen- and light-induced degradation.[64,65] Additionally, in presence of surface defects, light exposure can trigger the migration of iodine species from bulk to the surface leading to an intrinsic degradation of perovskite material.[49] In presence of an effective surface passivation, these effects can be mitigated, leading to increased intrinsic stability as previously observed.[67,68]

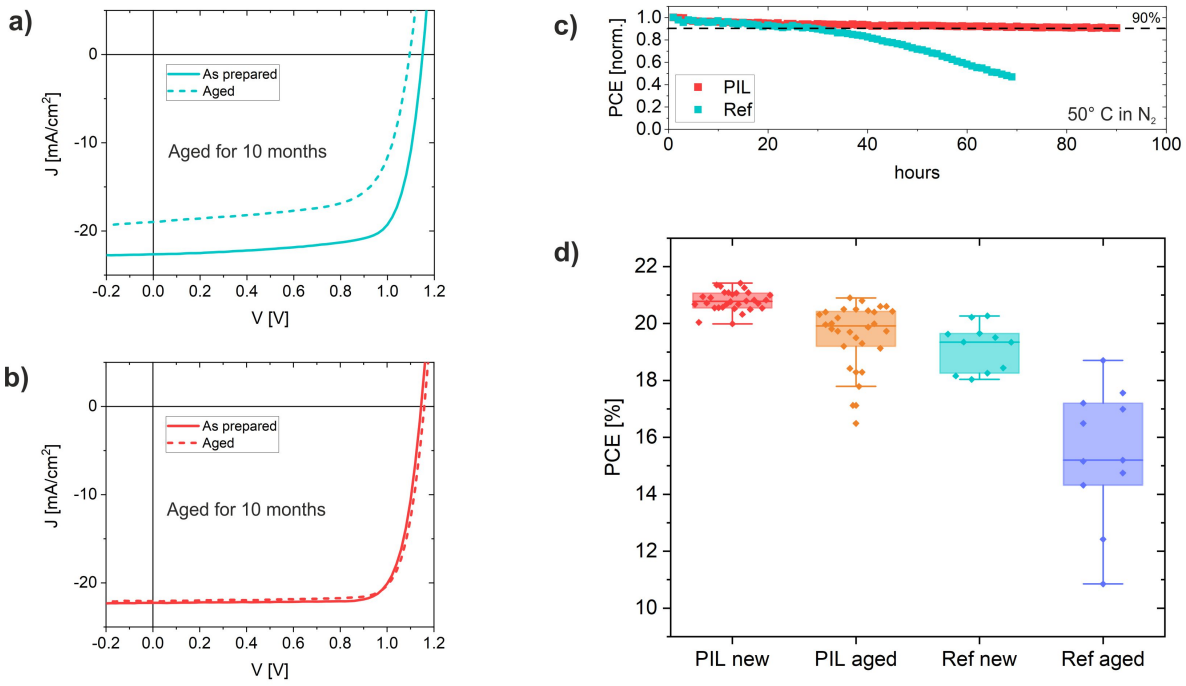

Figure 5: *a) and b) JV scans of as-prepared and 10 months aged reference and PIL treated devices. The samples were stored under N_2 atmosphere, non-encapsulated and exposed to indoor room light conditions. c) Maximum Power Point (MPP) tracking at 1 sun illumination conditions under N_2 atmosphere at 50°C for non-encapsulated devices with and without PIL. While the PCE of the reference device drops below 90% after roughly 20 h, the PIL device retains 90% of its efficiency even after 90h at MPP. d) Statistics of the PCE of the as-prepared (new) and aged (old) pin devices with and without PIL treatment. The aging time varies from 6 to 15 months, during which the samples were stored in nitrogen under room light.*

Finally, as a proof of concept, to corroborate the generality of this surface treatment, we expand our study to *nip* devices utilizing a lower bandgap perovskite (**Fig. S14, SI**). As in the *pin*-type cells, the PIL is deposited on top of the perovskite surface, but for this device structure being in contact with the Spiro-OMeTAD-based HTL. Surprisingly, also in this case, the introduction of the PIL at the perovskite/HTL interface results in an increased *FF*, from 70.19 ± 4 to 74.99 ± 1.4, and in enhanced reproducibility of the final devices. As for *pin* cells, the effective passivation of the perovskite surface upon PIL treatment results in a more ideal contact with the transport layers. However, in *nip* devices, the beneficial effects of the reduced interface recombination are less visible in terms of V_{OC} increase, only 20 mV, possibly due to the significant non-radiative recombination occurring at the perovskite/ETL interface, as reported recently.[63] Overall, these results highlight the versatility of this approach and open the door for this class of material to be explored in different device architectures and different perovskite compositions in the future.

Conclusions

In conclusion, we implemented an imidazolium-based poly-ionic liquid (PIL) with a bis(trifluoromethane)sulfonimide counterion [PeIm][TFSI] as a surface modifier of metal-halide perovskites in solar cells. Photoluminescence studies showed a significant reduction of the non-radiative recombination processes upon PIL treatment, both in the neat material and in full devices, resulting in a larger *QFLS* and longer carrier lifetimes. As a result, the device performance was significantly improved up to 21.4% through a concomitant increase in V_{OC} (1.17 V) and *FF* (up to 83%). Conductive AFM measurements revealed the bi-functional nature of this surface treatment, where on one side, polymer aggregates create insulating barriers while the neighbouring regions exhibit improved charge transfer properties. We propose that the ionic nature of the PIL enables charge compensation of surface defects, thereby homogeneously increasing the radiative efficiency of the neat perovskite and reducing charge carrier trapping. Photoemission spectroscopy studies highlighted a more ideal alignment between the perovskite and the C_{60} ETL, which improves charge extraction and the selectivity of the contact. Moreover, the combined effect of surface passivation and increased hydrophobicity improves the stability under MPP and during long-term shelf storage, allowing to retain unchanged PCE after 10 months. Finally, we demonstrated the generality of this concept by applying the same PIL to the top surface of the perovskite absorber in *nip*-type cells noting again enhanced *FF* and reproducibility. These results suggest that the surface modification induced by the PIL can improve both HTL and ETL interfaces and that its beneficial effect is not restricted to one type of device architecture. Overall, these findings may open the door to a wide usage of this class of material in combination with perovskite solar cells, potentially applicable to other perovskite compositions and tandem solar cells.

Acknowledgements:

The authors thanks Burkhard Stiller for performing the CAFM measurements. S.A. acknowledges funding from the German Federal Ministry of Education and Research (BMBF), within the project "Materialforschung für die Energiewende" (grant no. 03SF0540), and the German Federal Ministry for Economic Affairs and Energy (BMWi) through the "PersiST" project (grant no. 0324037C). Additional funding came from HyPerCells (a Joint Graduate School of the Potsdam University and the HZB) and by the Deutsche Forschungsgemeinschaft (DFG, German Research Foundation) – Project-ID 182087777 – SFB 951. G.G. acknowledges the "HY-NANO" project that has received funding from the European Research Council (ERC) Starting Grant 2018 under the European Union's Horizon 2020 research and innovation programme (Grant agreement No. 802862).

Author Contributions:

P. C. performed all the *pin* cell fabrication, photoluminescence studies, SEM, stability measurement and wrote the manuscript; D.S.C synthesised all the PILs and performed XRD and contact angle measurement; S.C.D. performed the EDX and CL measurements and analysis; F.Z. performed XPS and UPS measurements; A.A.S. and L.K. fabricated the *nip* devices; L.P.T. performed the conductivity measurements; C.M.W. helped during the stability measurements and assembled the experimental setup; N.K. supervised the XPS and UPS measurements and helped during the interpretation of the results; B.R. supervised the fabrication of *nip* cell at HZB and helped during the interpretation of the results; G.C. supervised the *nip* cell fabrication at EPFL and helped during the interpretation of the results; D.A. supervised the EDX and CL analysis and helped during the interpretation of the results; M.K.N. supervised the *nip* cell fabrication at EPFL and helped during the interpretation of the results; M.S. helped during photoluminescence measurements, the interpretation of the results and contributed in writing the manuscript; S.A. supervised all the work and helped during the interpretation of the results; M.A. supervised all the work and helped during the interpretation of the results; D.N. supervised all the work, helped during the interpretation of the results and contributed in writing the manuscript.

Competing Interests

The authors declare no competing interests.

Methods

***pin* Device Preparation:** Patterned indium-doped tin oxide (ITO, Lumtec, 15 ohm sqr.$^{-1}$) was washed with acetone, Hellmanex III, DI-water and isopropanol. After microwave plasma treatment (3 min at 200 W) poly[bis(4-phenyl)(2,4,6-trimethylphenyl)amine] (PTAA, Sigma-Aldrich, Mn = 7000–10000, PDI = 2–2.2) in a concentration of 1,5 mg/ml was spin-coated at 6000 rpm for 30 seconds and immediately annealed for 10 minutes at 100º C. The PTAA was additionally treated by dynamically spin coating a diluted solution (0.5mg/mL in Methanol) of poly[(9,9-bis(30- ((N,N-dimethyl)-N-ethylammonium)-propyl)-2,7-fluorene)- alt-2,7-(9,9-dioctylfluorene)] dibromide (PFN-P2). The perovskite layer was formed by spin coating a DMF:DMSO solution (4 :1 volume) at 4500 rpm for 35 seconds. After 10 seconds of spin coating, 300 mL of |Ethylacetate (antisolvent) was dripped on top of the spinning substrate. The perovskite is annealed for 2 minutes at 100º . The PIL is then spincoated on the perovskite, by spin coating a highly diluted solution (0.5 mg/ml in acetonitrile:isopropanol (1:4)). After deposition of the PIL the samples were annealed at 100º C for 1 h. Afterwards, samples were transferred to an evaporation chamber and C_{60} (30 nm), BCP (8 nm) and copper (100 nm) were deposited under vacuum (p =10^{-7} mbar). The active area was 6 mm^2 defined as the overlap of ITO and the top electrode.

***nip* Device Preparation: EPFL:** FTO-coated glass (Nippon sheet glass) was chemically etched with zinc powder and HCl solution, followed by sonically cleaning using Hellmanex, water, acetone, and 2-propanol. A 30 nm thick compact TiO_2 layer was deposited by spray pyrolysis of a titanium diisopropoxide bis(acetylacetonate) solution (Sigma-Aldrich) diluted in 2-propanol (1:15 v/v) at 450 °C. A 100 nm thick mesoporous TiO_2 layer was spin coated from a solution of TiO_2 paste (GreatCellSolar, 30NR-D) in ethanol (1:8 w/v) at 5000 rpm for 20 s followed by heating at 125 °C for 10 min and sintering at 500 °C for 20 min. A thin layer of passivating tin oxide of ≈20 nm was spin-coated by using tin (IV) chloride (Acros) solution (12 µL diluted in 988 µL water) at 3000 rpm for 30 s, followed by annealing at 100 °C for 10 min and 190 °C for 1 h. The prepared substrates were treated with UV-ozone for 15 min before perovskite deposition. A 1.3M $[(FAPbI_3)_{0.87}(MAPbBr_3)_{0.13}]_{0.92}(CsPbI_3)_{0.08}$ perovskite solution with excess PbI_2 (PbI_2:FAI = 1.05:1) was prepared by mixing FAI (GreatCellSolar), MABr (GreatCellSolar), CsI (ABCR), PbI_2 (TCI), and $PbBr_2$ (TCI) in DMF and DMSO (0.78:0.22 v/v). The prepared perovskite precursor was then spin-coated on the prepared at 2000 rpm for 12 s and 5000 rpm for 30 s. Chlorobenzene was added as an anti-solvent at 15 s before the end of spin coating process. The perovskite film was heated for 1h. After cooling down to the room temperature, the PIL layer was deposited on top of the perovskite layer at 6000 rpm for 30s, then the film was subsequently annealed at 100 °C for 60 min. Spiro OMeTAD was used as the hole-transporting materials (HTM). The HTM layer was prepared by dissolving 78.2 mg spiro-OMeTAD (Borun Chemical) in 1 mL chlorobenzene doped with 31.28 µL of 4-tert-butylpyridine (Sigma-Aldrich), 18.57 µL of Li-bis (trifluoromethanesulphonyl) imide (Aldrich) from the stock solution (196 mg in 379 µL acetonitrile), 13.69 µL of FK 209 Co(III) TFSI (GreatCellSolar) from the stock solution (99 mg in 263 µL acetonitrile). The doped spiro-OMeTAD solution was then deposited by spin-coating at 4000 rpm for 30 s. Finally, a 70 nm-thick gold counter electrode was thermally evaporated on top of HTM layer.

HZB: Planar *n-i-p* type perovskite solar cells were prepared as a layer stack of glass/ITO/SnO_2/$Cs_{0.05}((CH(NH_2)_2)_{0.83}(CH_3NH_3)_{0.17})_{0.95}Pb(I_{0.83}Br_{0.17})_3$/HTM/Au. Patterned ITO coated glass substrates (R = 15 Ω/sq., Automatic Research) were cleaned for 15 min each with detergent, acetone and isopropanol in an ultrasonic bath and subsequently treated for 15 min in a UV/O_3 cleaner. 22.5 mg/mL $SnCl_2 \cdot 2H_2O$ was dissolved in ethanol and stirred at room temperature overnight prior to spin coating 60 µl of the solution at 1500 rpm for 30 s. In a second step, another 60 µl of the $SnCl_2$ solution were dispersed on the substrate and rotated at 2500 rpm for 30 s before annealing at 180°C for one hour. After another UV/O_3 cleaning for 15 minutes, a KNO_3 solution (2.5 mg/ml in DI-H_20) was spin-coated onto the SnO_2 layer at 4000 rpm and annealed at 120°C for 10 minutes. Further layers were deposited in a N2 filled glovebox. $Cs_{0.05}(FA_{0.83}MA_{0.17})_{0.95}Pb(I_{0.83}Br_{0.17})_3$ perovskite was prepared from a precursor solution of FAI (1 M), PbI2 (1.1 M), MABr (0.2 M) and PbBr2 (0.2 M) in anhydrous DMF:DMSO 4:1 (v:v). Further, 5 mol-% CsI from a 1.5 M stock solution in DMSO was added to the precursor solution. The perovskite solution was spin coated in a two-step program at 1000 rpm for 10 s and 6000 rpm for 20 s. 5 s before to the end of the program, 160 µL of chlorobenzene was poured on the spinning substrate. Subsequently, the sample was annealed at 100 °C for 1 h. Next 36.2 mg of spiro-OMeTAD was dissolved in 1 mL of CBZ, 8.8 µL of a LiTFSI stock solution (520 mg/mL in acetonitrile), 14.5 µL of a FK209 stock solution (300 mg/mL in acetonitrile), and 14.4 µL of TBP. The doped spiro-OMeTAD solution was spin coated onto the samples at 1800 rpm for 30 s. Finally, 80 nm of gold were thermally evaporated at a base pressure of 10^{-6} mbar and a rate of 0.7 Å/s through shadow masks defining six active areas of 16 mm² per substrate.

Current Density–Voltage Characteristics, EQE_{PV} and 2-probe conductivity: J-V curves were measured under N_2 on a Keithley 2400 system in a 2-wire configuration with a scan speed of 0.1V/s and voltage step of 0.02V. One sun illumination at approximately 100mWcm^{-2} of AM1.5G irradiation was provided by a Oriel class ABA sun simulator. The real illumination intensity was monitored during the measurement using a Si photodiode and the exact illumination intensity was used for efficiency calculations. The sun simulator was calibrated with a KG5 filtered silicon solar cell (certified by Fraunhofer ISE). The AM1.5G short-circuit current of devices matched the integrated product of the EQE spectrum within 5-10% error. The latter was recorded using a home build set-up utilizing a Philips Projection Lamp (Type7724 12 V 100 W) in front of a monochromator (Oriel Cornerstone 74100) and the light was mechanically chopped at 70 Hz. The photo-generated current was measured using a lock-

in-amplifier (EG&G Princeton Applied Research Model 5302, integration times 300 ms) and evaluated after calibrating the lamp spectrum with an UV-enhanced Si photodetector (calibrated at Newport). The 2-probe conductivity was measured through current-voltage characteristics with an Agilent 4155C semiconductor parameter analyzer. The voltage was swept from positive to negative and the number of recorded points was kept at 201.

Absolute Photoluminescence: Excitation for the PL measurements was performed with a 445 nm CW laser (Insaneware) through an optical fibre into an integrating sphere. The intensity of the laser was adjusted to a 1 sun equivalent intensity by illuminating a 1 cm^2-size perovskite solar cell under short-circuit and matching the current density to the J_{SC} under the sun simulator (22.0 mA/cm^2 at 100 mWcm^{-2}, or 1.375x10^{21} photons $m^{-2}s^{-1}$). A second optical fiber was used from the output of the integrating sphere to an Andor SR393i-B spectrometer equipped with a silicon CCD camera (DU420A-BR-DD, iDus). The system was calibrated by using a calibrated halogen lamp with specified spectral irradiance, which was shone into to integrating sphere. A spectral correction factor was established to match the spectral output of the detector to the calibrated spectral irradiance of the lamp. The spectral photon density was obtained from the corrected detector signal (spectral irradiance) by division through the photon energy (hf), and the photon numbers of the excitation and emission obtained from numerical integration using Matlab. In a last step, three fluorescent test samples with high specified PLQY (~70%) supplied from Hamamatsu Photonics where measured where the specified value could be accurately reproduced within a small relative error of less than 5%.

Time Resolve Photoluminescence: Timeresolved PL data was acquired with a TCSPC system (Berger & Lahr) after excitation with a pulse-picked and frequency-doubled output from a mode-locked Ti:sapphire oscillator (Coherent Chameleon) with nominal pulse durations ~ 100fs and fluence of ~30nJ/cm² at a wavelength of 470nm.

Energy Disperisive X-Ray maps were acquired by means of an Oxford Instruments Ultim Extreme windowless X-ray detector in a Zeiss UltraPlus scanning electron microscope (SEM). Measurements were performed with an acceleration voltage of 3 kV and a beam current of about 10 pA.

Cathodoluminescence intensity maps were acquired by means of a Zeiss MERLIN SEM equipped with a SPARC system from Delmic. An aluminium parabolic mirror positioned above the sample focused the light into a photomultiplier tube (Thorlabs, PMT1001) outside the SEM chamber. We minimized the effect of beam damage by measuring under mild beam conditions (50 pA and 3.5 kV) and reduced electron dose (10 nm pixel size and 15 µs dwelling time per pixel).

Atomic Force Microscopy and Conductive Atomic Force Microscopy were performed with a Solver NT-MDT instrument with a hardware linearized 100 µm scanner and scanning tip. The measurements were performed in contact mode by measuring both spreading resistance and topography. The tip used was a platinum NSG10/Pt.

Contact Angle: The contact angle profile of CMB-TA on perovskite MAPI thin film were determined by droplet shape profile analysis from OCA instrument, data physics ES, Germany, and drop shape analysis dsa1 V1.80 Krüss software.

Poly-Ionic Liquid Synthesis

Materials

1-Vinylimidazole, 1-methylimidazole, ethylbromide, 4-vinylbenzyl chloride, water-soluble nonionic azo-initiator VA86 (WakeChemicals), and lithium bis(trifluoromethylsulfonyl)imide (TFSI; Aldrich 97%) were used as received without further purifications. All solvents used were of analytic grade.

IL-monomer synthesis(1-ethyl-3-vinilimidazolium bromide)
1-Vinylimidazole (4.7 g 0.05 M) were dissolved in 100 mL of methanol in a round bottom flask. Slowly addition of Ethyl bromide (6.5 g 0.06 M) while stirring further 1 hour. Then the solution was heated to 40 °C for 24 h. After the solution was cooled to room temperature, the white precipitate was washed with diethyl ether several times. Finally the precipitate was dried in a vacuum (1*10^{-3} mbar) oven. (Yield 90% , 9.1 g)

Polymer synthesis
The IL monomer (5.0 g) was dissolved in deionized water (50 mL) in a round bottom flask. After the monomer was dissolved, water-soluble nonionic azo-initiator VA86 (120 mg) was added. The mixture was purged with argon for 30 minutes and then stirred and heated to 85 °C for 24 h. After cooling to room temperature, the solution was precipitated into ice cooled THF (50 mL). A beige powder was filtered off and washed several times with THF. The dry powder was dried at 80°C under vacuum for 10 h. (3.0 g, 60%).

Ionic Exchange
The anion metathesis was performed by adding an aqueous solution of Li-TFSI (5.63 g, 20 mmol) into the aqueous solution of Br contained polymer to replace Br^- by $TFSI^-$. The resulting mixture was stirred for 1 h before filtering the solution using Por. 4 Buchner filter. The polymer was washed 5 times with water and dried in vacuum oven over night at 70 °C (2.1 g, 72%).

X-ray diffraction (XRD) patterns were obtained using Bruker D8 Advance X-ray diffractometer via Cu-K_α radiation.

X-ray and ultraviolet photoemission (XPS and UPS) measurements were conducted using a JEOL (JPS-9030) photoelectron spectrometer, which is equipped with a monochromatized Al Kα source (1486.6 eV) for XPS and hydrogen Lyman-α emission (10.2 eV) for UPS measurements.

Bibliography

1. Yin, W.-J., Shi, T. & Yan, Y. Unusual defect physics in CH 3 NH 3 PbI 3 perovskite solar cell absorber. *Appl. Phys. Lett* **104**, 063903 (2014).
2. De Wolf, S. *et al.* Organometallic halide perovskites: Sharp optical absorption edge and its relation to photovoltaic performance. *J. Phys. Chem. Lett.* **5**, 1035–1039 (2014).
3. Yin, W.-J., Yang, J.-H., Kang, J., Yan, Y. & Wei, S.-H. Halide perovskite materials for solar cells: a theoretical review. *J. Mater. Chem. A* **3**, 8926–8942 (2015).
4. Cai, M. *et al.* Cost-Performance Analysis of Perovskite Solar Modules. *Adv. Sci.* **4**, 1600269 (2017).
5. Green, M. A., Ho-Baillie, A. & Snaith, H. J. The emergence of perovskite solar cells. *Nat. Photonics* **8**, 506–514 (2014).
6. Hodes, G. Perovskite-Based Solar Cells. *Science (80-.).* **342**, 317–318 (2013).
7. Dong, Q. *et al.* Electron-hole diffusion lengths > 175 μm in solution-grown CH3NH3PbI3 single crystals. *Science (80-.).* **347**, 967–970 (2015).
8. Stranks, S. D. *et al.* Electron-Hole Diffusion Lengths Exceeding 1 Micrometer in an Organometal Trihalide Perovskite Absorber. *Science (80-.).* **342**, 341–344 (2013).
9. Braly, I. L. *et al.* Hybrid perovskite films approaching the radiative limit with over 90% photoluminescence quantum efficiency. *Nat. Photonics* **12**, 355–361 (2018).
10. Correa-Baena, J.-P. *et al.* Promises and challenges of perovskite solar cells. *Science* **358**, 739–744 (2017).
11. Tress, W. Perovskite Solar Cells on the Way to Their Radiative Efficiency Limit – Insights Into a Success Story of High Open-Circuit Voltage and Low Recombination. *Adv. Energy Mater.* **7**, 1602358 (2017).
12. Domanski, K., Alharbi, E. A., Hagfeldt, A., Grätzel, M. & Tress, W. Systematic investigation of the impact of operation conditions on the degradation behaviour of perovskite solar cells. *Nat. Energy* **3**, 61–67 (2018).
13. Noel, N. K. *et al.* Enhanced Photoluminescence and Solar Cell Performance via Lewis Base Passivation of OrganicÀInorganic Lead Halide Perovskites. **8**, 9815–9821 (2014).
14. Zheng, X. *et al.* Defect passivation in hybrid perovskite solar cells using quaternary ammonium halide anions and cations. *Nat. Energy* **2**, 17102 (2017).
15. Wolff, C. M. *et al.* Reduced Interface-Mediated Recombination for High Open-Circuit Voltages in CH 3 NH 3 PbI 3 Solar Cells. *Adv. Mater.* **29**, 1700159 (2017).
16. Deng, W., Liang, X., Kubiak, P. S. & Cameron, P. J. Molecular Interlayers in Hybrid Perovskite Solar Cells. *Adv. Energy Mater.* **8**, 1–20 (2018).
17. Caprioglio, P. *et al.* High open circuit voltages in pin-type perovskite solar cells through strontium addition. *Sustain. Energy Fuels* **3**, 550–563 (2019).
18. Abdi-Jalebi, M. *et al.* Maximizing and stabilizing luminescence from halide perovskites with potassium passivation. *Nature* **555**, 497–501 (2018).
19. Saliba, M. *et al.* Incorporation of rubidium cations into perovskite solar cells improves photovoltaic performance. *Science (80-.).* **354**, 206–209 (2016).

20. Klug, M. T. *et al.* Tailoring metal halide perovskites through metal substitution: influence on photovoltaic and material properties. *Energy Environ. Sci.* **236**, 236–246 (2017).

21. Bi, D. *et al.* Polymer-templated nucleation and crystal growth of perovskite films for solar cells with efficiency greater than 21%. *Nat. Energy* **1**, 16142 (2016).

22. Zuo, L. *et al.* Polymer-modified halide perovskite films for efficient and stable planar heterojunction solar cells. *Sci. Adv.* **3**, e1700106 (2017).

23. Wu, Q. *et al.* Solution-Processable Ionic Liquid as an Independent or Modifying Electron Transport Layer for High-Efficiency Perovskite Solar Cells. (2016). doi:10.1021/acsami.6b12683

24. Zhang, H. *et al.* Improved High-Efficiency Perovskite Planar Heterojunction Solar Cells via Incorporation of a Polyelectrolyte Interlayer. *Chem. Mater.* **26**, 5190–5193 (2014).

25. Grancini, G. & Nazeeruddin, M. K. Dimensional tailoring of hybrid perovskites for photovoltaics. *Nat. Rev. Mater.* **4**, 4–22 (2019).

26. Cohen, B.-E. El, Wierzbowska, M. & Etgar, L. High efficiency quasi 2D lead bromide perovskite solar cells using various barrier molecules. *Sustain. Energy Fuels* **1**, 1935–1943 (2017).

27. Etgar, L. The merit of perovskite's dimensionality; can this replace the 3D halide perovskite? *Energy Environ. Sci.* **11**, 234–242 (2018).

28. Cho, K. T. *et al.* Water-Repellent Low-Dimensional Fluorous Perovskite as Interfacial Coating for 20% Efficient Solar Cells. *Nano Lett* **18**, (2018).

29. Cho, K. T. *et al.* Highly efficient perovskite solar cells with a compositionally engineered perovskite/hole transporting material interface. *Energy Environ. Sci.* **10**, 621–627 (2017).

30. Grancini, G. *et al.* One-Year stable perovskite solar cells by 2D/3D interface engineering. *Nat. Commun.* **8**, 1–8 (2017).

31. Qiao, R. & Zuo, L. Self-assembly monolayers boosting organic-inorganic halide perovskite solar cell performance. *J. Mater. Res* **33**, 387–400 (2019).

32. Chang, C.-Y. *et al.* Achieving high efficiency and improved stability in large-area ITO-free perovskite solar cells with thiol-functionalized self-assembled monolayers. *J. Mater. Chem. A* **4**, 7903–7913 (2016).

33. Al-Ashouri, A. *et al.* Conformal monolayer contacts with lossless interfaces for perovskite single junction and monolithic tandem solar cells. *Energy Environ. Sci.* **12**, 3356–3369 (2019).

34. Christians, J. A. *et al.* Tailored interfaces of unencapsulated perovskite solar cells for >1,000 hour operational stability. *Nat. Energy* **3**, 68–74 (2018).

35. Jeon, N. J. *et al.* A fluorene-terminated hole-transporting material for highly efficient and stable perovskite solar cells. *Nat. Energy* **3**, 682–689 (2018).

36. Turren-Cruz, S.-H., Hagfeldt, A. & Saliba, M. Methylammonium-free, high-performance, and stable perovskite solar cells on a planar architecture. *Science (80-.).* **362**, 449–453 (2018).

37. Seo, J.-Y. Y. *et al.* Ionic Liquid Control Crystal Growth to Enhance Planar Perovskite Solar Cells Efficiency. *Adv. Energy Mater.* **6**, 1–6 (2016).

38. Wang, J. *et al.* Halide perovskite based on hydrophobic ionic liquid for stability improving and its application in high-efficient photovoltaic cell. *Electrochim. Acta* **303**, 133–139 (2019).

39. Xia, R. *et al.* Retarding Thermal Degradation in Hybrid Perovskites by Ionic Liquid Additives. *Adv. Funct. Mater.* **29**, 1902021 (2019).

40. Bai, S. *et al.* Planar perovskite solar cells with long-term stability using ionic liquid additives. *Nature* **571**, 245–250 (2019).

41. Yang, D. *et al.* Surface optimization to eliminate hysteresis for record efficiency planar perovskite solar cells. *Energy Environ. Sci.* **9**, 3071–3078 (2016).

42. Li, M. *et al.* Interface Modification by Ionic Liquid: A Promising Candidate for Indoor Light Harvesting and Stability Improvement of Planar Perovskite Solar Cells. *Adv. Energy Mater.* **8**, 1801509 (2018).

43. Wang, S. *et al.* Water-Soluble Triazolium Ionic-Liquid-Induced Surface Self-Assembly to Enhance the Stability and Efficiency of Perovskite Solar Cells. *Adv. Funct. Mater.* 1900417 (2019). doi:10.1002/adfm.201900417

44. Qian, W., Texter, J. & Yan, F. Frontiers in poly(ionic liquid)s: Syntheses and applications. *Chem. Soc. Rev.* **46**, 1124–1159 (2017).

45. Gao, M. R., Yuan, J. & Antonietti, M. Ionic Liquids and Poly(ionic liquid)s for Morphosynthesis of Inorganic Materials. *Chem. - A Eur. J.* **23**, 5391–5403 (2017).

46. Stolterfoht, M. *et al.* Approaching the fill factor Shockley–Queisser limit in stable, dopant-free triple cation perovskite solar cells. *Energy Environ. Sci.* **10**, 1530–1539 (2017).

47. Saliba, M. *et al.* Cesium-containing Triple Cation Perovskite Solar Cells: Improved Stability, Reproducibility and High Efficiency. *Energy Environ. Sci.* **9**, 1989–1997 (2016).

48. Stolterfoht, M. *et al.* Visualization and suppression of interfacial recombination for high-efficiency large-area pin perovskite solar cells. *Nat. Energy* **3**, 847 (2018).

49. Würfel, U., Neher, D., Spies, A. & Albrecht, S. Impact of charge transport on current-voltage characteristics and power-conversion efficiency of organic solar cells. *Nat. Commun.* **6**, (2015).

50. Luo, D. *et al.* Enhanced photovoltage for inverted planar heterojunction perovskite solar cells. *Science (80-.).* **360**, 1442–1446 (2018).

51. Yang, S. *et al.* Tailoring Passivation Molecular Structures for Extremely Small Open-Circuit Voltage Loss in Perovskite Solar Cells. *J. Am. Chem. Soc.* **141**, 5781–5787 (2019).

52. Yuan, J. & Antonietti, M. Poly(ionic liquid)s: Polymers expanding classical property profiles. *Polymer (Guildf).* **52**, 1469–1482 (2011).

53. Chen, B., Rudd, P. N., Yang, S., Yuan, Y. & Huang, J. Imperfections and their passivation in halide perovskite solar cells. *Chem. Soc. Rev.* **48**, 3842–3867 (2019).

54. Wang, Q. *et al.* Enhancing efficiency of perovskite solar cells by reducing defects through imidazolium cation incorporation. *Mater. Today Energy* **7**, 161–168 (2018).

55. Noel, N. K. *et al.* Enhanced Photoluminescence and Solar Cell Performance *via* Lewis Base Passivation of Organic–Inorganic Lead Halide Perovskites. *ACS Nano* **8**, 9815–9821 (2014).

56. Węcławik, M., Gągor, A., Piecha, A., Jakubas, R. & Medycki, W. Synthesis, crystal structure and phase transitions of a series of imidazolium iodides. *CrystEngComm* **15**, 5633 (2013).

57. Salado, M. *et al.* Towards Extending Solar Cell Lifetimes: Addition of a Fluorous Cation to Triple Cation-Based Perovskite Films. *ChemSusChem* **10**, 3846–3853 (2017).

58. Huang, C. *et al.* Ionic liquid modified SnO 2 nanocrystals as a robust electron transporting layer for efficient planar perovskite solar cells †. (2018). doi:10.1039/c8ta04131h

59. Zu, F. S. *et al.* Impact of White Light Illumination on the Electronic and Chemical Structures of Mixed Halide and Single Crystal Perovskites. *Adv. Opt. Mater.* **5**, 1700139 (2017).

60. Tseng, J.-K. *et al.* Interfacial polarization and layer thickness effect on electrical insulation in multilayered polysulfone/poly(vinylidene fluoride) films. *Polymer (Guildf).* **55**, 8–14 (2014).

61. Ganet, F. *et al.* Development of a smart guide wire using an electrostrictive polymer: option for steerable orientation and force feedback. *Sci. Rep.* **5**, 18593 (2016).

62. Caprioglio, P., Stolterfoht, M., Wolff, C. M., Unold, T. & Rech, B. On the Relation between the Open Circuit Voltage and quasi-Fermi Level Splitting in Efficient Perovskite Solar Cells. *Adv. Energy Mater.* 1901631 (2019). doi:10.1002/aenm.201901631

63. Stolterfoht, M. *et al.* The impact of energy alignment and interfacial recombination on the internal and external open-circuit voltage of perovskite solar cells †. *Energy Environ. Sci.* (2019). doi:10.1039/c9ee02020a

64. Ahn, N. *et al.* Trapped charge-driven degradation of perovskite solar cells. *Nat. Commun.* **7**, 13422 (2016).

65. Snaith, H. J. Perovskites: The Emergence of a New Era for Low-Cost, High-Efficiency Solar Cells. *J. Phys. Chem. Lett.* **4**, 3623–3630 (2013).

66. Motti, S. G. *et al.* Controlling competing photochemical reactions stabilizes perovskite solar cells. *Nat. Photonics* (2019). doi:10.1038/s41566-019-0435-1

67. Bryant, D. *et al.* Light and oxygen induced degradation limits the operational stability of methylammonium lead triiodide perovskite solar cells. *Energy Environ. Sci.* **9**, 1655–1660 (2016).

68. Pearson, A. J. *et al.* Oxygen Degradation in Mesoporous Al2O3/CH3NH3PbI3-xClx Perovskite Solar Cells: Kinetics and Mechanisms. *Adv. Energy Mater.* **6**, 1–10 (2016).

69. Rau, U. Reciprocity relation between photovoltaic quantum efficiency and electroluminescent emission of solar cells. *Phys. Rev. B* **76**, 085303 (2007).